



COF-C₄N Nanosheets with uniformly anchored single metal sites for electrocatalytic OER: From theoretical screening to target synthesis

Rui Zhang^{a,1}, Wenshan Liu^{a,1}, Feng-Ming Zhang^a, Zhao-Di Yang^{a,*}, Guiling Zhang^{a,*},
Xiao Cheng Zeng^{b,c,**}

^a Heilongjiang Provincial Key Laboratory of CO₂ Resource Utilization and Energy Catalytic Materials, School of Material Science and Chemical Engineering, Harbin University of Science and Technology, Harbin, Heilongjiang, 150080, China

^b Department of Chemistry, University of Nebraska-Lincoln, Lincoln, NE 68588, United States

^c Department of Materials Science & Engineering, City University of Hong Kong, Kowloon, Hong Kong, China

ARTICLE INFO

Keywords:

Covalent organic framework
Single metal atom catalysts
Descriptor
Electrocatalytic OER performance
Experimental verification

ABSTRACT

COF-C₄N, an effective oxygen evolution reaction (OER) electrocatalyst with a low overpotential, has ideal N-edge cavities for anchoring transition metal (TM) sites to achieve single atom catalysts (SACs) with higher OER activity. To screen out the optimal TM, two descriptors for characterizing the OER activities are proposed based on systematic density-functional theory calculations for two different classes of COF, TM-COF-C₄N and TM-Aza-CMP. Among them, Co-COF-C₄N and Ni-COF-C₄N are theoretically suggested to be highly active and low-cost OER SACs for target synthesis. Followed by a series of structural characterizations (PXRD, XPS, FT-IR, EXAFS, ICP, TEM and SEM) as well as OER performance measurement, it is confirmed that Co-COF-C₄N exhibits excellent OER activity with an overpotential of 280 mV at 10 mA cm⁻², more active than most of previously reported OER electrocatalysts. The molecular mechanism underlying the high activity is explored.

1. Introduction

Efficient electrocatalytic water splitting is one of effective carbon-free approaches to attain renewable energy for addressing the global warming issue [1–3]. The oxygen evolution half-reaction is known to be the bottleneck in the water splitting due to its four-electron transfer reaction pathway with relatively low efficiency and high-energy input [4–6]. For the development of highly active OER electrocatalysts, a variety of homogeneous and heterogeneous catalysts with different conversion efficiency and selectivity have been studied [7–10]. In recent years, two-dimensional covalent organic frameworks (2D-COFs), a new class of crystalline and porous organic materials assembled by covalent connection of building block, has emerged as promising candidates for OER electrocatalysis, owing to their diverse, well-defined, and long-range-order structures with ample binding sites for anchoring metal atoms, as well as large surface-to-volume ratios [11–14]. Electrochemical active 2D-COFs, such as metalloporphyrin [15,16], metal-phthalocyanine [17,18] and metal coordinated COFs [19–22],

have been shown to possess stable active sites for OER and exhibit desirable low overpotential. Most of these 2D-COFs are assembled by metalloporphyrin (-phthalocyanine) or coordinated with metal atoms. Only a few metal-free 2D-COFs can serve as efficient electrocatalysts for OER due to the lack of catalytic active center to overcome sluggish OER kinetics [23–25]. Single atom catalysts (SACs) with high stability, activity, and selectivity for water splitting [26,27] have attracted intense attention. 2D-COF can be an ideal substrate for anchoring single metal sites due to its high chemical stability and N-rich structures, thereby potentially serving as highly efficient and tunable SACs through modulating the electronic structure of catalytic center [13,26–32]. For example, TpBPY-COF, when simultaneously coordinated by Fe and Co sites, can be an electrocatalyst for OER with the overpotential of 1.59 V @ 10 mA cm⁻² [31]. Therefore, it is timely to examine catalytic OER performance of different active metal sites on 2D-COFs in order to develop optimal 2D-COF based SACs.

COF-C₄N nanosheets have been previously synthesized and investigated by us through the reaction of triphenylenehexamine (TPHA) and

* Corresponding authors.

** Correspondence to: Department of Materials Science & Engineering, City University of Hong Kong, Kowloon, 999077, Hong Kong, China.

E-mail addresses: yangzhaodi@163.com (Z.-D. Yang), guiling-002@163.com (G. Zhang), xzeng26@cityu.edu.hk (X.C. Zeng).

¹ These authors contributed equally to this work.

hexaketocyclohexane (HKH) by using a solvothermal method [33,34]. It has been shown that the metal-free COF-C₄N nanosheets exhibit good OER performance with a low overpotential of 349 mV @ 10 mA cm⁻² and a Tafel slope of 64 mV dec⁻¹. As such, the catalytic activities of COF-C₄N nanosheets are superior to most other metal-free OER electrocatalysts, and are even comparable to some metal-embedding COFs, but are weaker than conventional metal/precious metal electrocatalysts. Nevertheless, because transition metal (TM) atoms can be favorably anchored at native N-edge cavities of COF-C₄N via the formation of two TM-N covalent bonds, and TM-anchored COF-C₄N can maintain the planar structure. In other words, the pristine COF-C₄N can become an ideal substrate for anchoring active TM sites and be converted into highly efficient SACs for OER. To date, COF-C₄N based SACs have not been explored systematically like graphene supported SACs [35,36]. Theoretical screening based on rational design principle would be a cost-effective approach for the development of efficient SACs but also could offer molecular insights into generic trend on active sites and activity-enhancement factors for different TM sites anchored at native N-edge cavities of COF-C₄N. Especially, effective theoretical descriptors, once validated with experiments, will be useful for quick assessment of electrocatalytic activities of the COF-C₄N based SACs.

Herein, we report a joint theoretical/experimental study of the structure-activity relationship for a series of TM ion (from Sc to Cd) anchored on the COF-C₄N monolayer (TM-COF-C₄N) as OER electrocatalysts (see Fig. 1a). Two theoretical descriptors are examined to be effective, including a ϕ parameter and the free energy difference $\Delta G_3 - \Delta G_2$ associated with the OER reaction. Both descriptors can be viewed as

generic ones for predicting the OER activity of various single TM atom anchored porous materials with native N-edge cavities, such as Aza-CMP. The descriptor-based theoretical screening suggests that the Ni, Co and Fe are the optimal and low-cost TMs with high catalytic activities when anchored on COF-C₄N nanosheets. Subsequent experiments on OER performance confirm that the Co-COF-C₄N nanosheets are likely the most active OER catalyst among the three nanosheets.

2. Computational and experimental details

2.1. Computational details

2.1.1. Computational method and details

The density functional theory (DFT) calculations are performed by using the Vienna ab initio simulation package (VASP)[37,38]. The interaction between the core and valence electrons is described using the frozen-core projector augmented wave (PAW) approach [39,40]. The generalized gradient approximation of Perdew-Burke-Ernzerhof (PBE) functional [41] is used. The energy cutoff is set to be 500 eV. A Γ -centered mesh of $3 \times 3 \times 1$ k-points is used to sample the two-dimensional Brillouin zone. The van der Waals (vdW) correction proposed by Grimme is adopted to describe long-range vdW interactions [42]. A vacuum space greater than 15 Å perpendicular to the sheet is applied so that the interaction between neighboring slabs is negligible. All geometry structures are fully relaxed until the convergence criteria of energy and force are less than 10^{-5} eV and 0.01 eV Å⁻¹, respectively.

The binding energy (E_b) of the transition metal (TM) complexed on

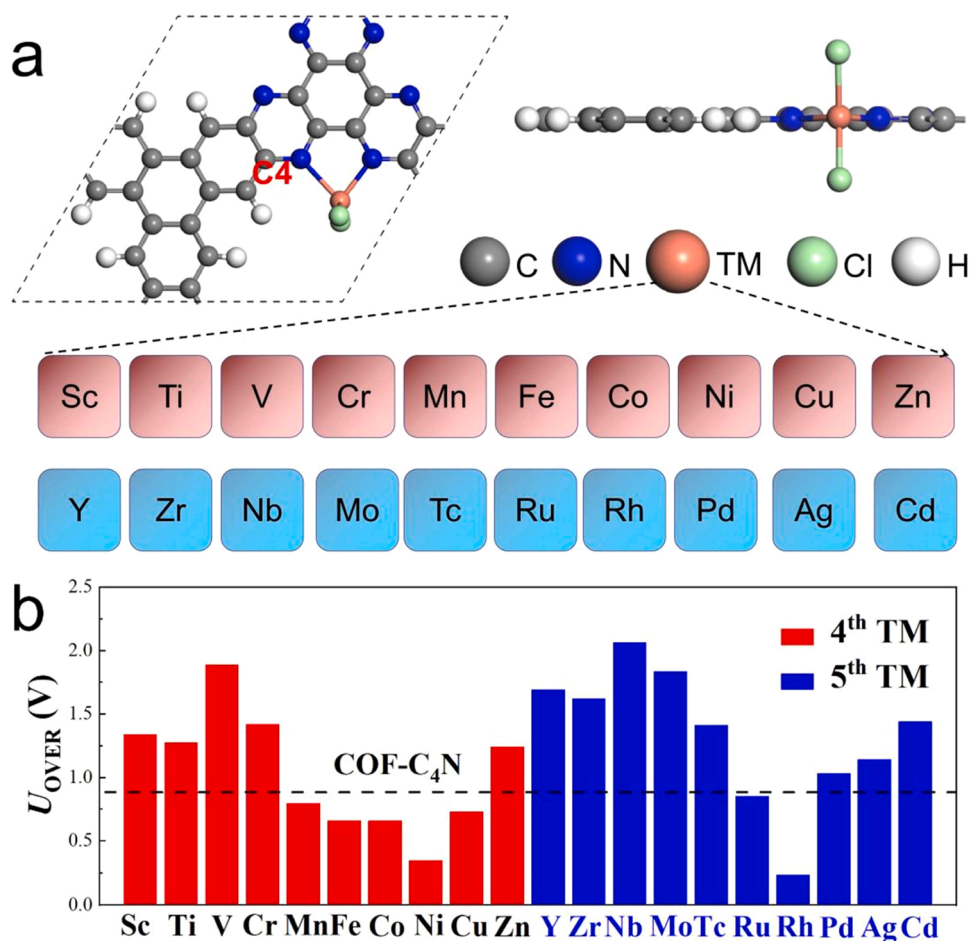


Fig. 1. (a) Unit cell structure of TM-COF-C₄N in top and side views. Atom labels: C (gray), N (blue), H (white), Cl (green) and TM (orange). The TM atoms (considered from Sc to Cd) are listed. (b) A summary of computed overpotentials on TM-COF-C₄N for OER, where the red column represents the 4th period TM and the blue column represents the 5th period TM, respectively. The dashed line represents the overpotential of the metal-free pristine COF-C₄N.

the COF-C₄N monolayer is calculated according the formula given below:

$$E_b = E_{\text{TM-COF-C}_4\text{N}} - E_{\text{C}_4\text{N}} - E_{\text{TMCl}_x(x=1,2\text{or}3)} \quad (1)$$

where $E_{\text{TM-COF-C}_4\text{N}}$ is the total energy of the TM-COF-C₄N, $E_{\text{C}_4\text{N}}$ and $E_{\text{TMCl}_x(x=1, 2 \text{ or } 3)}$ are the energies of the COF-C₄N monolayer and TM chlorides, respectively.

2.1.2. Calculation of free energy difference

The free energy difference for OER is calculated according to the computational hydrogen electrode model originally proposed by Nørskov and coworkers [43,44]:

$$\Delta G = \Delta E + \Delta E_{\text{ZPE}} - T\Delta S + \Delta G_{\text{pH}} + \Delta G_{\text{U}} \quad (2)$$

In Eq. (2), ΔE is the difference in electronic energy before and after adsorption, taken directly from the DFT calculations, and ΔE_{ZPE} and ΔS are the zero-point energy correction and entropy change between the adsorbed state and gas state, obtained from frequency calculations at 298 K, respectively. For computing thermodynamic properties, the thermodynamic conditions are set to be 1 atmosphere and 298 K. The pH dependence of the reduction potential is given by $\Delta G_{\text{pH}} = 0.059 \times \text{pH}$, which stems from the H^+ concentration dependence of the entropy [45]. ΔG_{U} is the contribution of the applied electrode potential (U) to ΔG . The equilibrium potential U_0 for OER at pH = 0 is determined to be 1.23 V vs computational hydrogen electrode (CHE), where the reactant and product are at the same energy level. The onset potential (U_{onset}) is defined as the applied potential (U) required to keep every elemental step exothermic. The overpotential (U_{OVER}) is defined as the onset potential minus the ideal equilibrium potential 1.23 V. They can be obtained from the free energy change in the rate-determining step (RDS) and defined as follow:

$$U_{\text{onset}} = -\Delta G_{\text{max}}/e \quad (3)$$

$$U_{\text{OVER}} = U_{\text{onset}} - U_0 \quad (4)$$

OER involves four electrons steps, which can be written as Step1–4 oxidation reaction equations:



where * denotes the adsorption site, *OH, *O and *OOH denote the adsorbed intermediate species.

Considering the contribution from the zero-point energy, the entropy, the pH dependence of the redox potential, and the external potential supplied by carrier, the free-energy changes along reaction pathway for OER can be expressed as:

$$\Delta G_{*OH} = G_{*OH} + 1/2G_{\text{H}_2} - G_* - G_{\text{H}_2\text{O}} - \Delta G_{\text{pH}} - eU \quad (5)$$

$$\Delta G_{*O} = G_{*O} + G_{\text{H}_2} - G_{\text{H}_2\text{O}} - G_* - 2\Delta G_{\text{pH}} - 2eU \quad (6)$$

$$\Delta G_{*OOH} = G_{*OOH} + 3/2G_{\text{H}_2} - G_* - 2G_{\text{H}_2\text{O}} - 3\Delta G_{\text{pH}} - 3eU \quad (7)$$

$$\Delta G_{\text{O}_2} = 2G_{\text{H}_2} + G_{\text{O}_2} - 2G_{\text{H}_2\text{O}} - 4\Delta G_{\text{pH}} - 4eU \quad (8)$$

Here, various intermediate states along the reaction paths are calculated based on the consideration of the adsorption of free radicals or atoms on the material surface. Entropy values of the molecules (H_2 and H_2O) are taken from the standard tables in Physical Chemistry [46]. The free energy of $\text{O}_2(\text{g})$ is derived as:

$$G_{\text{O}_2} = 2G_{\text{H}_2\text{O}} - 2G_{\text{H}_2} + 4.92\text{eV} \quad (9)$$

The free energy changes of each step can be related to (5) to (8) by:

$$\Delta G_1 = \Delta G_{*OH} \quad (10)$$

$$\Delta G_2 = \Delta G_{*O} - \Delta G_{*OH} \quad (11)$$

$$\Delta G_3 = \Delta G_{*OOH} - \Delta G_{*O} \quad (12)$$

$$\Delta G_4 = 4.92\text{ eV} - \Delta G_{*OOH} \quad (13)$$

2.2. Materials synthesis

2.2.1. Synthesis of COF-C₄N

C₃-symmetric 2, 3, 6, 7, 10, 11-triphenylhexamine 6 HCl (TPHA, 25.5 mg, 0.08 mmol) and C₃ symmetric hexaketo cyclohexane octahydrate (HKH, 25.0 mg, 0.08 mmol), 1.5 mL 1,4-dioxane and 1.5 mL 1,3,5-trimethylbenzene are put into a 10 mL tube. The mixture is sonicated at 25 °C for 30 min, and then 4 mL aqueous acetic acid solution (0.5 mL) is added to the test tube. The tube is degassed using three freeze-pump-thaw cycles and then sealed and kept in an air-dry oven at 150 °C for 3 days. The precipitate is filtered and thoroughly cleaned by Soxhlet extraction with tetrahydrofuran and acetone respectively. Finally, it is freeze-dried at 120 °C under reduced pressure (−0.09 MPa) for 12 h.

2.2.2. Loading of Co(II) into COF-C₄N

Co-COF-C₄N is synthesized by impregnating COF-C₄N in methanol solution containing Co(OAc)₂ precursor. Reaction system with Co(II) is given below as an example. 30 mg cobalt acetate is dissolved in 100 mL methanol, and then 30 mg COF-C₄N is dispersed in methanol solution of cobalt acetate. After ultrasonic treatment for 30 min, the COF-C₄N is completely dispersed. The solution is stirred for 12 h at room temperature. Filter the solution and obtain a filter cake. The filter cake is washed thoroughly with water and ethanol to remove any free metal ions. The final filter cake is dried at 100 °C under dynamic vacuum for overnight to get Co-COF-C₄N.

2.2.3. Loading of Ni(II) /Fe(II) /Mn(II) /Cu(II) into COF-C₄N

Ni-COF-C₄N, Fe-COF-C₄N, Mn-COF-C₄N and Cu-COF-C₄N are synthesized following the synthetic procedure as for Co-COF-C₄N.

2.3. Characterizations

All solvents and reagents are obtained from commercial sources without further purification. The structure, composition and texture properties of the materials are studied by using powder X-ray (PXRD) diffraction (Bruker D8 X-ray diffractometer), Fourier transform infrared (FT-IR) (Spectrum 100), thermogravimetric analyses(TGA) (SDTA851e), scanning electron microscopy (SEM) micrographs (Hitachi S-4800), transmission electron microscopy (TEM) experiment (JEM-2100 electron microscope). X-ray photoelectron spectroscopy (XPS) measurements are using ESCALAB 250Xi from Thermo SCIENTIFIC and the C1s peak at 284.6 eV as internal standard. Inductively Coupled Plasma (ICP) analysis is undertaken using the Inductively Coupled Plasma Atomic Emission Spectrometer (iCap7400). Before the measurement, the sample is first degassed at 120 °C for 12 h.

2.4. Electrochemical measurements

All electrochemical measurements are performed at room temperature on the Chi660e electrochemical workstation with standard three electrode channels. The three electrode device includes catalyst coated carbon fiber cloth as working electrode, Ag/AgCl (saturated KCl) as reference electrode and carbon electrode as counter electrode. All potential measurements are converted to the RHE according to the following formula $E_{\text{vs RHE}} = E_{\text{vsAg/AgCl}} + E_{\text{Ag/AgCl}}^0 + 0.059\text{ pH}$ (in volts)

[47]. Linear scan voltammetric curves (LSVs) of OER are obtained in nitrogen saturated KOH solution at 1600 rmp speed and 5 mV s^{-1} scanning speed. The overpotential is obtained according to the following equation: $\eta = E_{\text{RHE}} - 1.23 \text{ V}$ [48]. Calculation of the Tafel slope according to Tafel equation: $\eta = \log j + a$, where η is the overpotential (V), j is the current density (mA cm^{-2}), and b is the Tafel slope (mV dec^{-1}) [49]. The CVs of the samples are measured in 1 M KOH solution at scanning rates (20, 40, 60, 80 and 100 mV s^{-1}) to compare the effective electrode surface area (ECSA) of the relevant samples [50]. Electrochemical impedance spectroscopy (EIS) is tested in potentiostatic mode of 1.579 V vs. RHE (@ 10 mA cm^{-2}), with OER ranging from 100 kHz to 0.1 Hz and applied voltage amplitude of 5 mV. Electrochemical testing is carried out under the standard three electrode system. The prepared samples are used as the working electrode, platinum plate (99.9%) as counter electrode, saturated KCl Ag / AgCl electrode as the reference and 0.5 M Na_2SO_4 solution as electrolyte. All experiments are carried out at room temperature and 1 atm, and before the experiment, high pure nitrogen is used to make bubbles through the electrolyte.

3. Results and discussion

3.1. Computed overpotentials and two descriptors

Most of TM-COF-C₄N are produced via TMCl_2 coordinating to two N atoms of COF-C₄N, while some special TM-COF-C₄N are formed by TMCl or TMCl_3 coordinating to native N-edge cavities to be the most stable structures, shown in Fig. 1a. The geometrical optimization for all TM-COF-C₄Ns is performed based on the DFT method. The calculated binding energies of COF-C₄N monolayer and TM chlorides and associated bond length of TM-N are also calculated and summarized in Supporting Information (Table S1). The binding energies, ranging from -6.45 to -1.30 eV, and the TM-N bond lengths, ranging from 1.94 to 2.44 Å, indicate the TM will be localized stably in the cavity of COF-C₄N.

For metal-free COF-C₄N, the sp^2 -hybridized C4 sites are considered as the optimal OER active sites (The optimal C4 site is confirmed in our previous work [33] by comparing 4 kinds of C sites). Our DFT calculations show that the OER rate-determining step is the third oxidation step ($\text{*O} \rightarrow \text{*OOH}$) and the computed overpotential of the COF-C₄N is 0.884 eV. For TM-COF-C₄N, the TM site is the more active site compared to the sp^2 -hybridized C site. The adsorption of intermediates (*OH , *O and *OOH) on all TM-COF-C₄Ns is optimized by using the DFT method, and the free energies of adsorption for the three intermediates are computed. The free energy profiles associated with the OER pathway at $U = 0$ and $U = 1.23 \text{ V}$ for all TM-COF-C₄Ns are given in Figs. S1 and S2. The rate-determining step can be TM dependent for all TM-COF-C₄Ns, and the corresponding theoretical overpotentials (U_{OVER}) are shown in Fig. 1b, in which the U_{OVER} is defined as $U_{\text{OVER}} = -\Delta G_{\text{max}}/e - 1.23 \text{ V}$ (details in Computational Section in Section 2.1.2). The theoretical overpotential of the metal-free COF-C₄N is taken as a standard as marked by a dashed line in Fig. 1b. It is clear that the U_{OVER} values of 4th period TM (red column) and 5th period TM (blue column) show similar fluctuating trend with the increasing of atomic number. Compared with the U_{OVER} of the metal-free COF-C₄N, seven TM-COF-C₄Ns with TM = Mn, Fe, Co, Ni, Cu, Ru and Rh exhibit a lower U_{OVER} , suggesting these seven TM-COF-C₄Ns may exhibit enhanced OER catalytic activity.

To determine intrinsic and key factors that affect the catalytic activity of TM-COF-C₄N, the relationship between the catalytic center and the overpotential is explored. A descriptor ϕ similar to the one previously proposed [35] for evaluating the OER activity of graphene supported SACs is considered here. This descriptor recognizes the fact that the filling electrons in the occupied d orbital (θ_d) of TM in the TM-COF-C₄N structure play an important role to regulate the overpotential of OER. In particular, the filling d electrons of TM atoms can affect the electron transfer between TM d orbital and p orbital of adsorbates, thereby influencing the binding strength of the adsorbates to

TM during OER process. For example, the Fe(II) with $\theta_d = 6$ can play an important role to the catalytic activity of the Fe-containing catalysts [51]. In addition, to account for the redistribution of θ_d due to the interaction among TM, the adsorbate, the coordinated nearby atoms, and the electronegativity of these TM atoms are also included in the descriptor ϕ . It is known that the electronegativity measures the electron affinity of elements when the relevant covalent bond is formed. The electronegativity of the metal atom and coordinated atoms would effectively enhance the value of θ_d , while the electronegativity of the atom of adsorbate (O atom for OH^*) attached to TM would effectively reduce the value of θ_d . Considering these key factors, the extended descriptor ϕ is written as the following:

$$\phi = \alpha \theta_d \times \frac{E_M + (n_N \times E_N + n_{\text{Cl}} \times E_{\text{Cl}})}{E_O} \quad (14)$$

where E_M , E_{Cl} , E_N and E_O are the electronegativity of the transition metal, chlorine, nitrogen and oxygen elements, respectively, n_{Cl} and n_N represent the number of the nearest-neighbor Cl and N atoms, θ_d denotes filling electrons number in the d orbitals of TM, and α is the correction coefficient. Specifically, $\alpha = 1$ for 4th period TM elements. For the early five TM elements in the 5th period, Y, Zr, Nb, Mo, and Tc, with relatively larger atomic radius, each $4d$ orbital is only occupied by one electron (the d -orbital electron configurations for all TM ions are shown in Table S2). Thus, the stronger d - p_z coupling between the TM d state and N p_z state tends to emerge in TM-COF-C₄N for these early TM elements in the 5th period. The strong d - p_z coupling effect and the lack of paired electrons in the d orbitals of early TM elements result in delocalized π electrons which can easily transfer from COF-C₄N to the TM, in comparison with the late five TM elements in the 5th period. As such, the ability to accept electrons from the radicals during the OER would be weakened for Y, Zr, Nb, Mo, and Tc. For Ru, Rh, Pd Ag and Cd (the late five TM elements in the 5th period), and they are less affected by the delocalized π electrons in the COF-C₄N due to more electrons filling in the $4d$ orbitals. As such, these TM sites would be easier to accept electrons during OER. The correction coefficient α seems related to the ratio of C and N content in the substrate (e.g., 2D-COF). Tuning the ratio of C and N content of the substrate could regulate the electrochemical activity, because the amount of delocalized π electrons in the 2D-COF sheet is correlated with its N content. With the increase of N content in the 2D-COF sheet, more delocalized π electrons can transfer from supported sheet to TM atoms, lowering the overpotential of OER while promoting the adsorption and reaction kinetics of the intermediates. Since the ratio of C and N for the COF-C₄N is 4:1, α is set to 1/4 for the early TM elements, Y, Zr, Nb, Mo, and Tc; and $\alpha = 1$ for the late TM elements in the 5th period.

Filling electrons in the d orbital (θ_d), electronegativity and the corresponding descriptor ϕ of TM-COF-C₄N with different coordination environment are listed in Table S2. In Fig. 2a, the calculated descriptor ϕ is plotted versus the overpotential of TM-COF-C₄N. After data collection and linear fitting, a piecewise linear relationship of ϕ versus U_{OVER} is obtained, resembling an inverted volcano with the zenith for ϕ being 32.1.

For $\phi > 32.1$, the ϕ versus U_{OVER} can be correlated by a straight line with a regression coefficient $R^2 = 0.83$, while for $\phi < 32.1$ the linear correlation with U_{OVER} yields $R^2 = 0.83$ also. Here, the OER activity is enhanced with increasing ϕ . For $\phi = 32.1$, the TM-COF-C₄N exhibits the optimal OER activity. The volcano relationship between ϕ and U_{OVER} reinforces the effects of the d -orbital electrons and coordination environment on the electronegativity. Based on the previously reported d band center model [52,53], the adsorption strength of a TM is closely related to its d -band structure, a notion also is taken into account in the descriptor ϕ . To show more clearly which TM-COF-C₄Ns exhibit enhanced OER catalytic activity than COF-C₄N, the U_{OVER} of COF-C₄N is taken as a reference (i.e., a black dashed line in Fig. 2a). The black dashed line cuts the volcano plot into a zone from 21.37 to 36.62, in

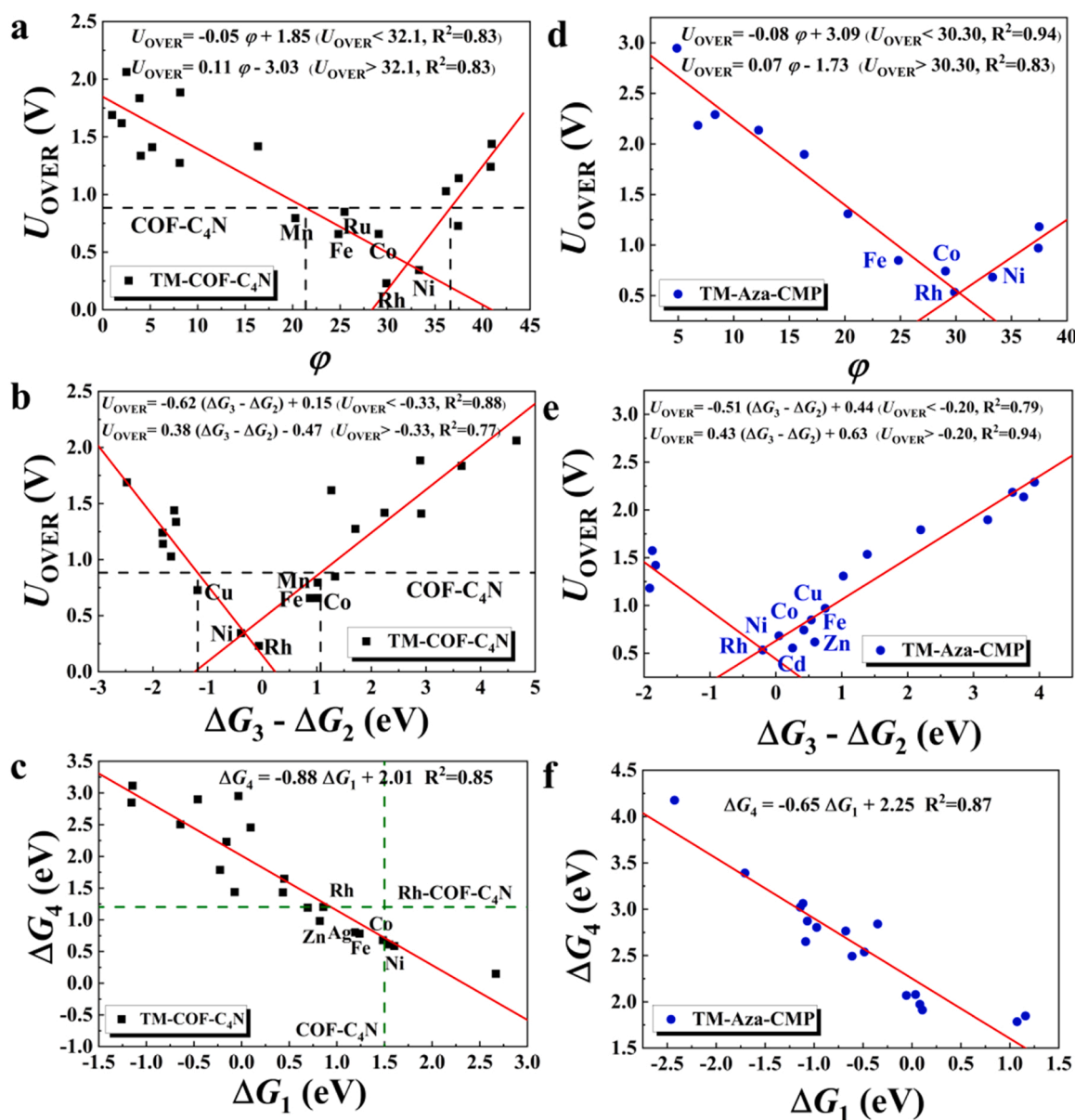


Fig. 2. (a) Overpotentials versus the descriptor ϕ ; (b) Overpotentials versus $\Delta G_3 - \Delta G_2$ for all TM-COF-C₄N; (c) Linear relationship between ΔG_1 and O₂ desorption free energies ΔG_4 for TM-COF-C₄N. (d) Overpotentials versus the descriptor ϕ ; (e) Overpotentials versus $\Delta G_3 - \Delta G_2$ for TM sites anchored Aza-CMP and (f) linear relationship between ΔG_1 and O₂ desorption free energies ΔG_4 for TM sites anchored Aza-CMP, respectively.

which Rh, Ni, Co, Fe and Ru are identified as the potential TMs for SAC with enhanced catalytic activity over the pristine COF-C₄N.

Besides the inverted volcano relationship between ϕ and U_{OVER} , an inverted volcano relationship between the free energy change $\Delta G_3 - \Delta G_2$ and U_{OVER} is also identified, as illustrated in Fig. 2b. Here, the inverted volcano exhibits a zenith at -0.33 eV. Compared reference value (U_{OVER} of the pristine COF-C₄N), the range for improving the catalytic activity is from -1.18 – 1.07 eV, in which Rh, Ni, Co, Fe and Mn based TM-COF-C₄Ns would show enhanced OER catalytic properties over COF-C₄N. Considering both inverted volcano relationships (in Fig. 2a-b), Rh, Ni, Co and Fe are identified as the four potential TMs for the TM-COF-C₄N based SAC.

Next, we consider the adsorption and desorption of species relevant to OER on TM-COF-C₄N. Here, the first step and last step are analyzed with a linear regression, and a favourable R^2 linear regression coefficient of 0.85 is obtained, as illustrated in Fig. 2c. This fitting result suggests the higher values of ΔG_{OH} (ΔG_1) could result in the lower energy barrier in the step 4 from $^*\text{OOH}$ to O₂. But it does not mean higher ΔG_1 is

better. The ΔG_1 value of the pristine COF-C₄N is set as another reference as marked by a vertical green dashed line in Fig. 2c. Those TM-COF-C₄Ns on the left of the green dashed line show lower ΔG_1 relative to pristine COF-C₄N, suggesting the corresponding TMs are the more active sites than the C sites on TM-COF-C₄N. In addition, among all the TM-COF-C₄Ns, the lowest U_{OVER} is given by the Rh-COF-C₄N. The ΔG_4 of Rh-COF-C₄N is also set as a reference marked as the horizontal green dashed line. Those TM-COF-C₄Ns below the horizontal green dashed line tend to desorb O₂ easier than Rh-COF-C₄N. The elements Co, Ni, Fe, Ag and Zn are below the horizontal green dashed line, suggesting they would possess reasonable adsorption and desorption capability for OER. Thus, combining the two descriptors and the linear relationship between adsorption and desorption, the non-precious TMs, Ni, Co and Fe, are opted as the optimal single TM sites anchored on COF-C₄N by forming two TM-N coordination bonds at native N-edge cavities. The OER activity is predicted to be Ni(II) > Co(II) > Fe(II).

3.2. Extension of the descriptors to other SAC systems

To examine whether the proposed descriptors ϕ and $\Delta G_3 - \Delta G_2$ can be extended to predict the OER activity of other SACs with native N-edge cavities, the TM atoms anchored Aza-CMP (C_5N_2) are constructed and the corresponding OER pathways are calculated (Fig. S3). As the ratio of C/N in the Aza-CMP is 5:2, α is set to be 2/5 for TM-Aza-CMP. According to Formula 14, the computed descriptors ϕ of TM-Aza-CMPs (C_5N_2) also adopts the same correlation coefficient α , that is, $\alpha = 1$ for 4th period TM. For 5th period TM, α is set to 2/5 for the early five TMs, while $\alpha = 1$ for the late TMs. Similarly, the ϕ versus U_{OER} can be nicely correlated by straight lines with a regression coefficient of $R^2 = 0.83$ or 0.94 (Fig. 2d). The $\Delta G_3 - \Delta G_2$ versus U_{OER} , as illustrated in Fig. 2e, presents the same inverted volcano relationship for TM-Aza-CMP with a zenith at -0.2 . The corresponding overpotentials follow the same distribution trend as suggested by the descriptors ϕ and $\Delta G_3 - \Delta G_2$, suggesting that both descriptors can be quite generic for SAC systems with native N-edge cavities. According to the descriptors, Co atom anchored Aza-CMP with a low U_{OER} of 0.75 eV is a highly active SAC which has been verified by the experiment (289 mV at 10 mA cm^{-2} and 1 M NaOH [54]). Moreover, the adsorption and desorption energies for species involved in OER on TM-atom anchored Aza-CMP are also analyzed by a linear regression with a good regression coefficient, as shown in Fig. 2f. This result confirms the high correlation between adsorption and desorption step in OER. Thus, both ϕ and $\Delta G_3 - \Delta G_2$ are proposed as two efficient descriptors for the prediction of the catalytic activity of SACs with single TM atoms localized in the N-edge cavity.

3.3. Experimental confirmation

To verify the theoretical predictions, target synthesis of Co-COF-C₄N, Ni-COF-C₄N and Fe-COF-C₄N SACs has been carried out, while Mn-COF-C₄N and Cu-COF-C₄N are also prepared for comparison. First, COF-C₄N is synthesized via the reaction of C₃-symmetric 2,3,6,7,10,11-triphenylenehexamine (TPHA) and HKH using the previously reported method [33]. Next, TM-COF-C₄N is synthesized by impregnating COF-C₄N in methanol solution with the $M(\text{OAc})_2$ precursor (Fig. 3). Notably, both the theoretical prediction and the measured OER performance show that Ni-COF-C₄N and Co-COF-C₄N exhibit higher OER activities. To better understand the higher activities, structure characterizations, OER performance, and mechanistic study of Ni-COF-C₄N and Co-COF-C₄N are mainly reported below.

The crystalline structures of Co-COF-C₄N, Ni-COF-C₄N and COF-C₄N are characterized by powder X-ray diffraction (PXRD). As shown in Fig. 4a, the PXRD of as-synthesized COF-C₄N (blue line) shows sharp diffraction peaks at 7.2° and 27° , which can be assigned to the (100) and (001) facets, respectively. After chelating $M(\text{OAc})_2$, the PXRD patterns of Co-COF-C₄N and Ni-COF-C₄N exhibit no significant changes

compared with the parental COF-C₄N. Based on the FT-IR analysis as shown in Fig. 4b, the formation of phenazine linkages with characteristic bands at 1509 , 1458 , and 1389 cm^{-1} is detected for COF-C₄N, Co-COF-C₄N and Ni-COF-C₄N, indicating that the rigid structure of phenazine bond of the original COF-C₄N remains intact. The new stretch at 1560 and 1440 cm^{-1} can be assigned to the acetate group (COO^- tensile band). Both PXRD and FT-IR results indicate that the TM anchored at native N-edge cavities of COF-C₄N by $M(\text{OAc})_2$ coordination do not change the framework and interlayer space of crystalline COF-C₄N.

X-ray photoelectron spectroscopy (XPS) measurement shown in Fig. 4c demonstrates the presence of C, N, O and Co (Ni) in Co-COF-C₄N (Ni-COF-C₄N). Analyzing the N 1s XPS of Co-COF-C₄N (Ni-COF-C₄N) in Fig. 4d, the N-C corresponds to 398.5 eV (398.6 eV), N = C corresponds to 400.0 eV (399.7 eV), N-Co corresponds to 401.1 eV, and N-Ni corresponds to 400.3 eV, confirming that the metal Co and Ni are successfully coordinated on the pyridine N sites of native N-edge cavities. The O 1s XPS spectra of Co-COF-C₄N and Ni-COF-C₄N show the existence of Co-O and Ni-O bond (Fig. 4e). For Co-COF-C₄N in Fig. 4f, the binding energy of the Co 2p $1/2$ and Co 2p $3/2$ appear at 797.1 and 782.4 eV, the Co 2p $3/2$ peak at 782.4 eV is shifted from 784.3 eV of pure cobalt acetate, indicating the formation of coordination bond between Co (II) and two pyridine N sites in the native N-edge cavities on COF-C₄N. For Ni-COF-C₄N, the Ni 2p $1/2$ and Ni 2p $3/2$ peaks appear at 872.1 eV and 854.5 eV, respectively, and the Ni 2p $3/2$ peak is shifted from 855.5 eV of nickel acetate to 854.5 eV, indicating the formation of coordination bond between Ni (II) and two pyridine N sites in the native N-edge cavities. All XPS results verify the anchoring of Co(II) and Ni(II) onto COF-C₄N. The normalized Co K-edge XANES spectrum, the raw and fitted k^2 -weighted EXAFS spectra for Co-COF-C₄N are given in Fig. 4g, 4h and 4i, and the EXAFS fitting parameters at the Co K-edge sample are shown in Table S3, further confirming that Co-COF-C₄N is a single TM-atom anchored catalytic system with the Co (II) tetracoordinated with two N and two O (Fig. 4g).

Fig. 5a–b, d–e shows the transmission electron microscopy (TEM) image of the synthesized Co-COF-C₄N and Ni-COF-C₄N, respectively. The regular pores and well-knit stripes could be seen clearly from TEM at 10 nm magnification, indicating a hierarchical structure and nearly perfect π – π compact stacking between layers. This structure is consistent with the graphene-like hexagonal honeycomb structure. It can be seen that the loading of metal site has no effect on the pores and morphology of the original COF-C₄N. The distances between the layers of the Co-COF-C₄N or layers of Ni-COF-C₄N are 3.36 Å or 3.4 Å. Scanning electron microscopy (SEM) measurement also shows the agglomerated nanosheet morphology of Co-COF-C₄N and Ni-COF-C₄N (Fig. 5c and 5f). Clearly, the metal ions and N atoms are evenly distributed in the COF-C₄N skeleton. The amount of Co^{2+} coordinated into COF-C₄N is quantified by inductively coupled plasma (ICP). It reveals an average metal content of 9.77 (wt.)% (Table S4). COF-C₄N and Co-COF-C₄N are

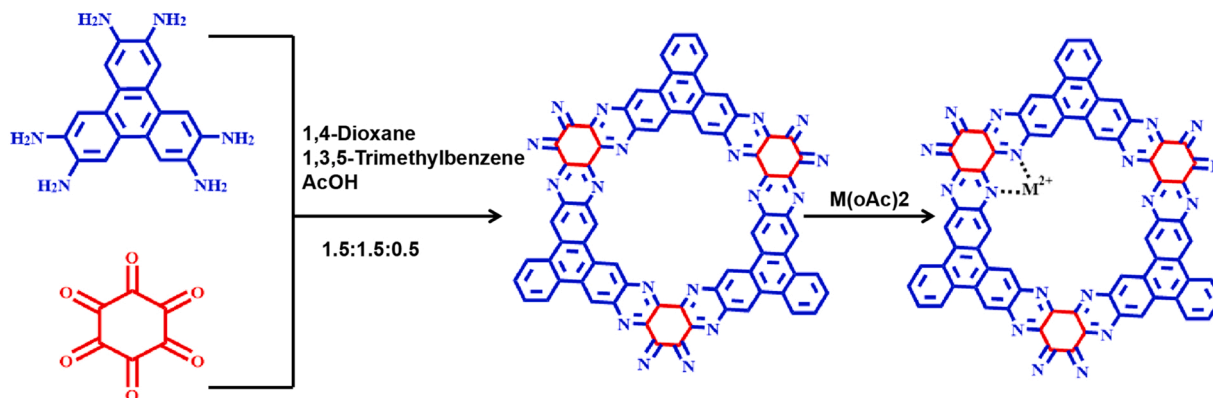


Fig. 3. Schematic illustration of the TM-COF-C₄N synthesis.

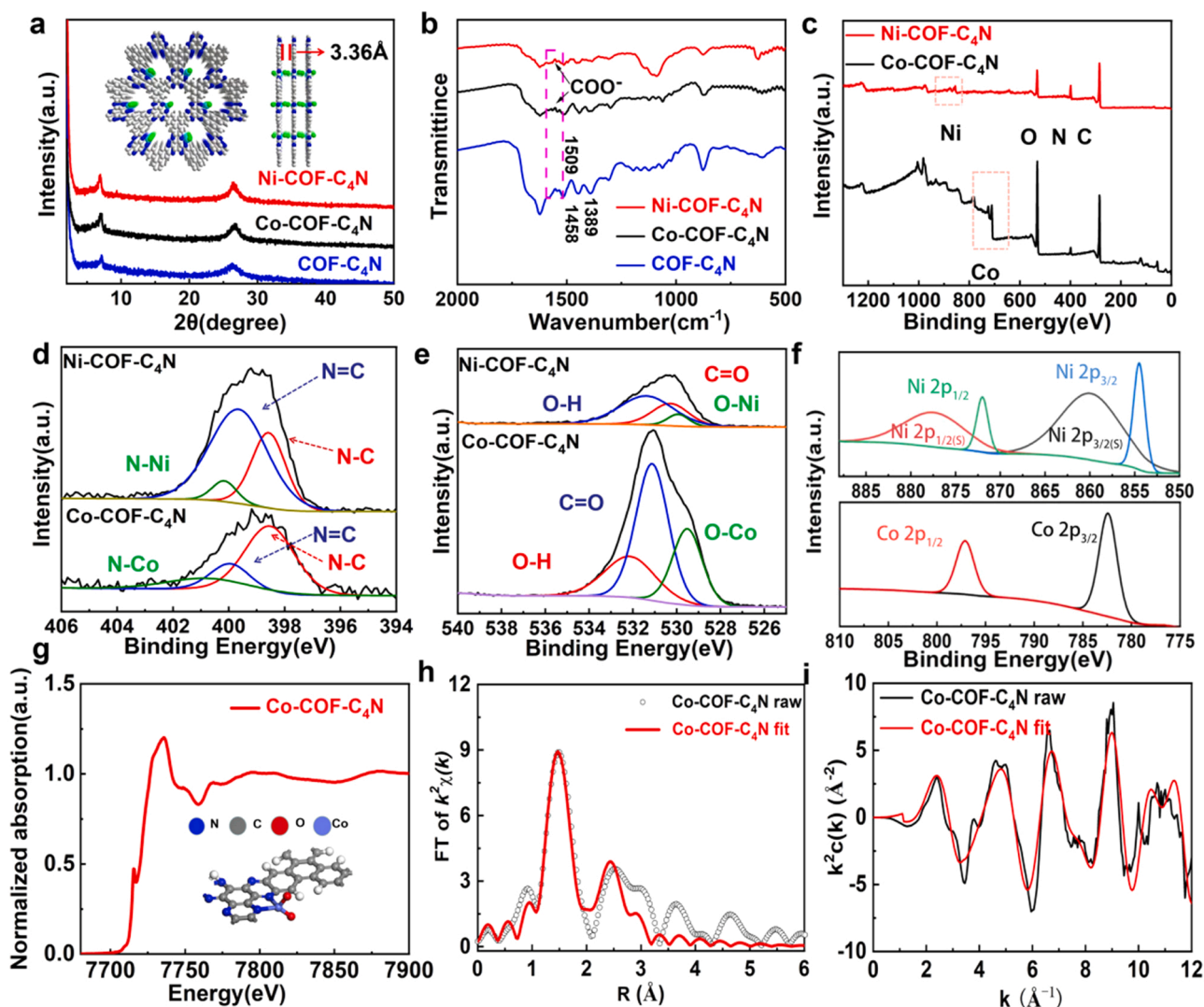


Fig. 4. (a) PXRD patterns of COF-C₄N (blue), Co-COF-C₄N (black) and Ni-COF-C₄N (red); (b) FT-IR spectra of COF-C₄N (blue), Co-COF-C₄N (black) and Ni-COF-C₄N (red); (c) XPS profile of Co-COF-C₄N (black) and Ni-COF-C₄N (red); (d) N 1s, (e) O 1s and (f) Ni 2p and Co 2p XPS spectra of Co-COF-C₄N and Ni-COF-C₄N; (g) normalized Co K-edge XANES spectrum of Co-COF-C₄N (Inset is the unit-cell structure of Co²⁺ anchored COF-C₄N with coordination number of 4, including two N and two O); (h, i) experimental and fitted k^2 -weighted Co K-edge EXAFS curves of Co-COF-C₄N.

tested by Thermogravimetric analysis (TGA) as shown in Fig. S4. The result demonstrates thermal stability up to 594 °C and 638 °C with weight loss of 30% under N₂ atmospheres for COF-C₄N and Co-COF-C₄N, respectively. On the basis of above results and analysis, Co (II) and Ni (II) are successfully and uniformly anchored on COF-C₄N.

Next, the traditional standard three-electrode channel is used to perform the electrochemical tests. The three electrode devices are carbon fiber cloth coated with catalyst as working electrode, Ag/AgCl (saturated KCl) as the reference electrode and carbon electrode as the counter. The linear sweep voltammograms (LSVs) curves of Co-COF-C₄N, Ni-COF-C₄N, Fe-COF-C₄N, Mn-COF-C₄N and Cu-COF-C₄N are given in Fig. 6, as well as the C₄N-COF, A-B and C-C for comparison. The overpotentials of Co-COF-C₄N, Ni-COF-C₄N and Fe-COF-C₄N are lower than that of COF-C₄N, but Mn-COF-C₄N and Cu-COF-C₄N give higher overpotentials than COF-C₄N. The experimental results well validate the theoretical predictions and the design strategy of COF-C₄N based SACs to enhance OER activity.

We also carried out LSV test for different mass ratio of Co-COF-C₄N and Ni-COF-C₄N as shown in Fig. S5. Compared with COF-C₄N, the measured overpotential of Co-COF-C₄N 1:1 (feed ratio of Co(OAc)₂ and COF-C₄N) is 280 mV at 10 mA cm⁻² (Fig. 7a), 69 mV lower than that of

COF-C₄N. And it can provide a current density up to 399 mA cm⁻², two times higher than that of COF-C₄N and thus superior to the vast majority of reported OER electrocatalysts (Table S5). The overpotential of Ni-COF-C₄N 20:1 (feed ratio of Ni(OAc)₂ and COF-C₄N) also notably decreases (307 mV at 10 mA cm⁻²) as shown in Fig. 7a.

To elaborate the advantages of Co-COF-C₄N and Ni-COF-C₄N, the Tafel slopes of COF-C₄N, Co-COF-C₄N 1:1 and Ni-COF-C₄N 20:1 are shown in Fig. 7b, derived from the corresponding LSV curves. The Tafel slope gives a value of 43 mV dec⁻¹ for Co-COF-C₄N 1:1, 69 mV dec⁻¹ for Ni-COF-C₄N 20:1, and 65 mV dec⁻¹ for COF-C₄N, suggesting that Co-COF-C₄N 1:1 results in more effective charge transfer at the electrode-electrolyte contact. At 10 mA cm⁻², we use simple cyclic voltammetry (CV) to estimate the relative differences in the surface area of electrochemical activity (Fig. S6 and S7). And the obtained current density is plotted as a function of scan rate in Fig. 7c. Clearly, the electrochemical double-layer capacitance value for Co-COF-C₄N 1:1 and Ni-COF-C₄N 20:1 is about 8 times and 4 times larger, respectively, compared to COF-C₄N. The increase of the electrochemical active surface area indicates that the TM sites contribute to the improved catalytic performance. Electrochemical impedance spectroscopy (EIS) measurement is carried out to study the electrode-electrolyte kinetics under the OER conditions.

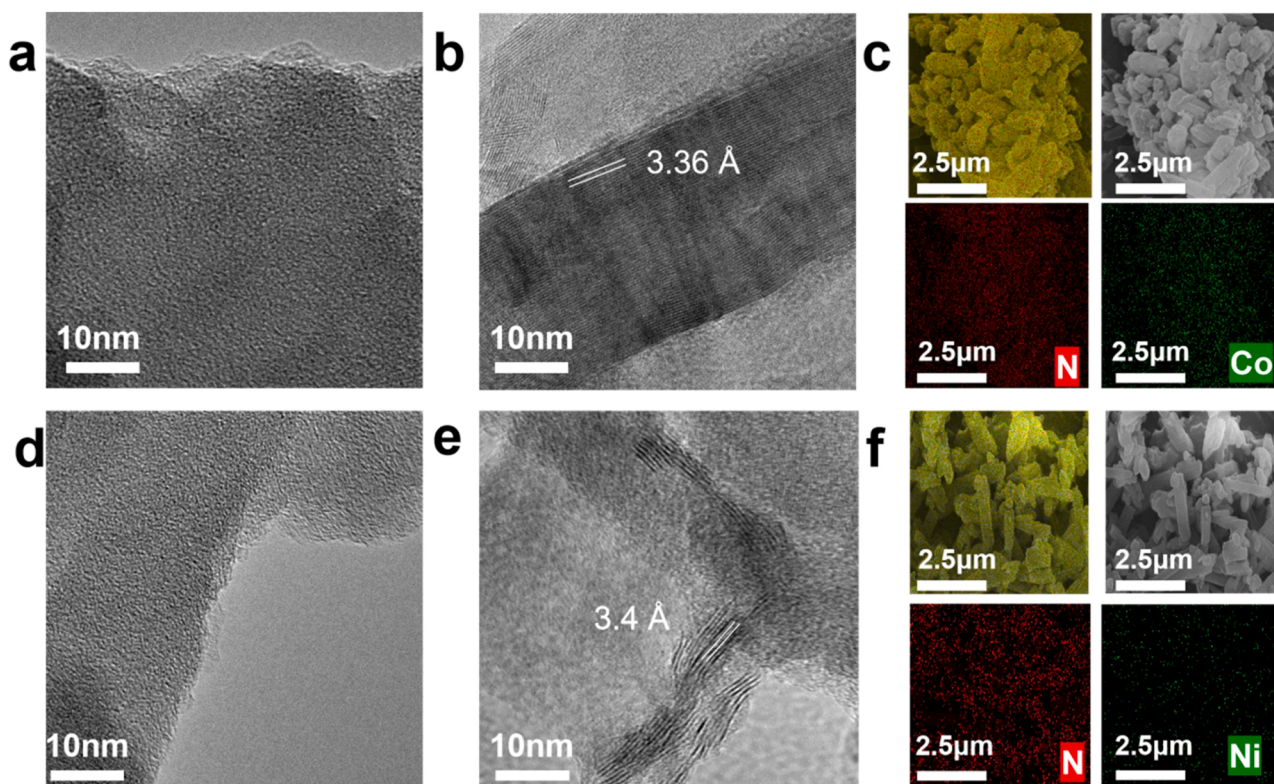


Fig. 5. (a–b) TEM images of Co-COF-C₄N; (d–e) TEM images of Ni-COF-C₄N; (c) SEM image of Co-COF-C₄N and mixed element map and mappings of N and Co; (f) SEM image of Ni-COF-C₄N and mixed element map and mappings of N and Ni.

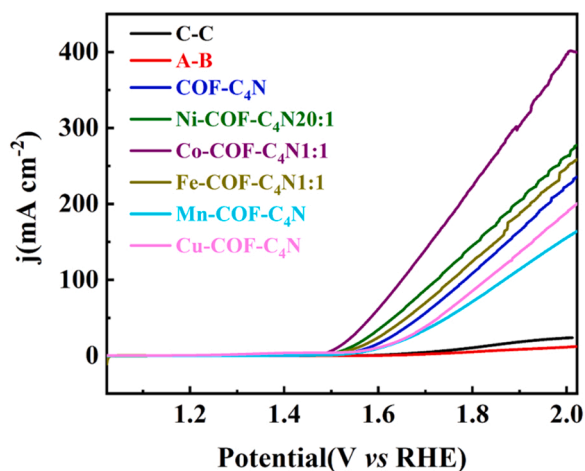


Fig. 6. LSV curves of the different metal-modified M-COF-C₄N and the pristine COF-C₄N.

The Nyquist plots (Fig. 7d) demonstrate that the interfacial charge transfer resistance of Co-COF-C₄N 1:1 and Ni-COF-C₄N 20:1 are significantly lower than that of COF-C₄N at 0.6 V, which could be correlated with their improved conducting properties, charge transfer, and separation. The electrochemical stability of the Co-COF-C₄N 1:1 is tested from chronoamperometry measurements which indicate that the catalytic current density decreases to 93.5% after 20 h continuous measurement (Fig. S8). It shows excellent electrocatalytic stability.

After electrocatalytic stability test, the PXRD pattern of tested Co-COF-C₄N 1:1 is characterized again (Fig. S9). It still shows diffraction peaks at 7.2° and 27°. XPS, TEM and SEM results of the tested Co-COF-C₄N 1:1 are given in Fig. S10 and S11, which also show good structural

stability after 20 h chronoamperometric durability test. Considering both theoretical predictions and experimental results, we conclude that Co (II) is likely the best non-precious metal atom to be anchored at native N-edge cavities of COF-C₄N as OER SAC.

To further explore the mechanism of Co and Ni metal site for promoting OER activity, the free energy profiles of OER pathway at $U = 0$ V and the experimental applied potential bias for Co-COF-C₄N and Ni-COF-C₄N are calculated and shown in Fig. 8. From the OER pathway at $U = 0$ V, one can see that the rate-determining step (RDS) is the third step $*O \rightarrow *OOH$ ($\Delta G_3 = 1.88$ eV) for Co-COF-C₄N and the second step $*OH \rightarrow *O$ ($\Delta G_2 = 1.57$ eV) for Ni-COF-C₄N. The theoretical onset potential U equals to the free energy change of RDS according to the Eq. (3). Supporting Information Due to a higher free energy change in the rate-determining step for Co-COF-C₄N (1.89 eV), the OER reaction of Co-COF-C₄N should require a higher onset potential bias U to reduce the free energy change so that it could be overcome easily at room temperature. However, the experimentally applied potential bias is 1.510 V and 1.536 V for Co-COF-C₄N and Ni-COF-C₄N, respectively. As shown in Fig. 8, both Co-COF-C₄N and Ni-COF-C₄N show a reasonable downhill trend at realistically applied bias U , and the ΔG of each step of Co-COF-C₄N at $U = 1.510$ V is a little lower than that of Ni-COF-C₄N at $U = 1.536$ V, suggesting that the OER of Co-COF-C₄N would be faster under the potential bias. The theoretical prediction of the OER activity trend is not entirely consistent with the experimental results for Co-COF-C₄N and Ni-COF-C₄N, as the charge transfer should be considered in addition to the OER pathway of active sites.

Lastly, we show the computed electronic properties of $*OOH$ intermediate of Co-COF-C₄N and Ni-COF-C₄N. The partial density of states (PDOS), crystal orbital Hamilton population (COHP), and charge density difference between $*OOH$ and the TM site for Co-COF-C₄N and Ni-COF-C₄N are shown in Fig. 9. The computed PDOS suggests that the O 2p states are strongly coupled with metal 3d states near the Fermi level for both Co-COF-C₄N and Ni-COF-C₄N, and they are mainly contributed by the O p_y (O p_x) and 3d_{yz} (3d_{xz}). The interaction between the metal 3d

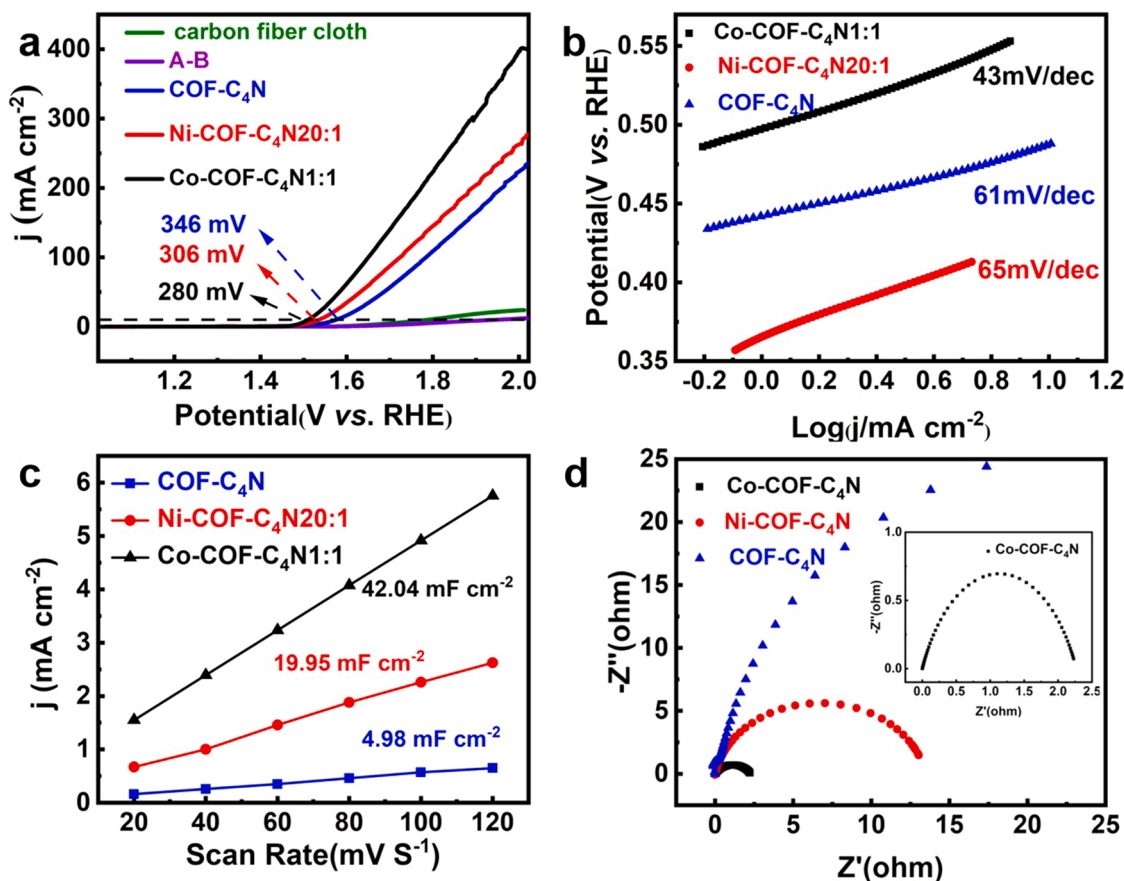


Fig. 7. (a) LSVs for OER in a N₂-saturated 1.0 M KOH aqueous solution. (b) Tafel plots obtained from OER polarization curves. (c) Capacitive currents versus scan rates on the basis of CV curves recorded at different scan rates. (d) EIS Nyquist comparison plots.

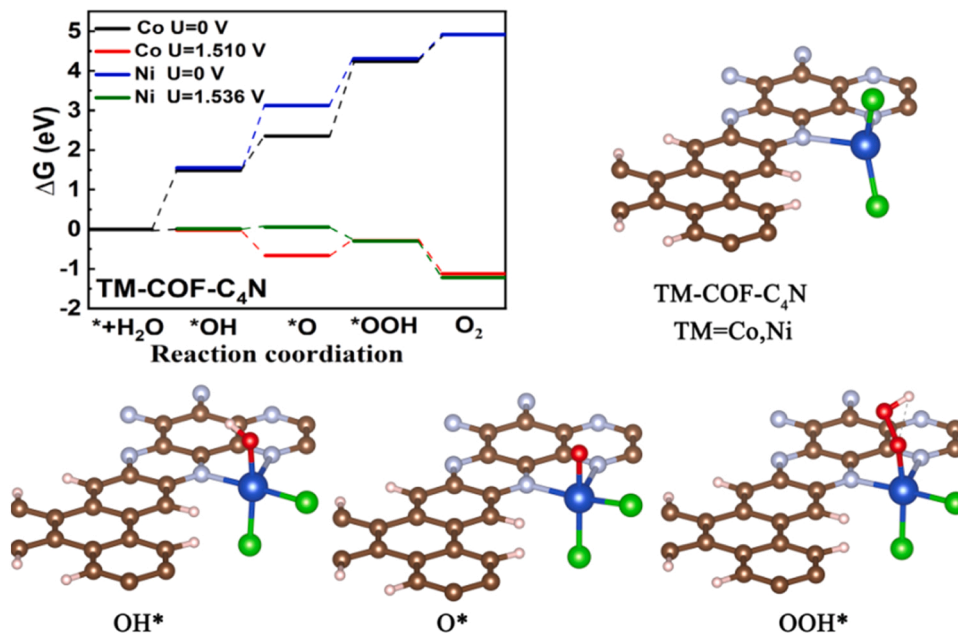


Fig. 8. The free energy profile of OER pathway at the applied potential bias and $U = 0$ for Co-COF-C₄N and Ni-COF-C₄N. The structures of *OH, *O and *OOH intermediates.

orbitals and O 2p orbitals renders the hybridized energy level lowered than the Fermi level, resulting in the antibonding population below E_F (see the crystal orbital Hamilton population (COHP) in Fig. 9b and e).

The *OOH adsorption strength is determined by the filling population of the bonding states. The adsorption strength is weakened when more antibonding states are below E_F . [55,56] Compared to Ni-COF-C₄N,

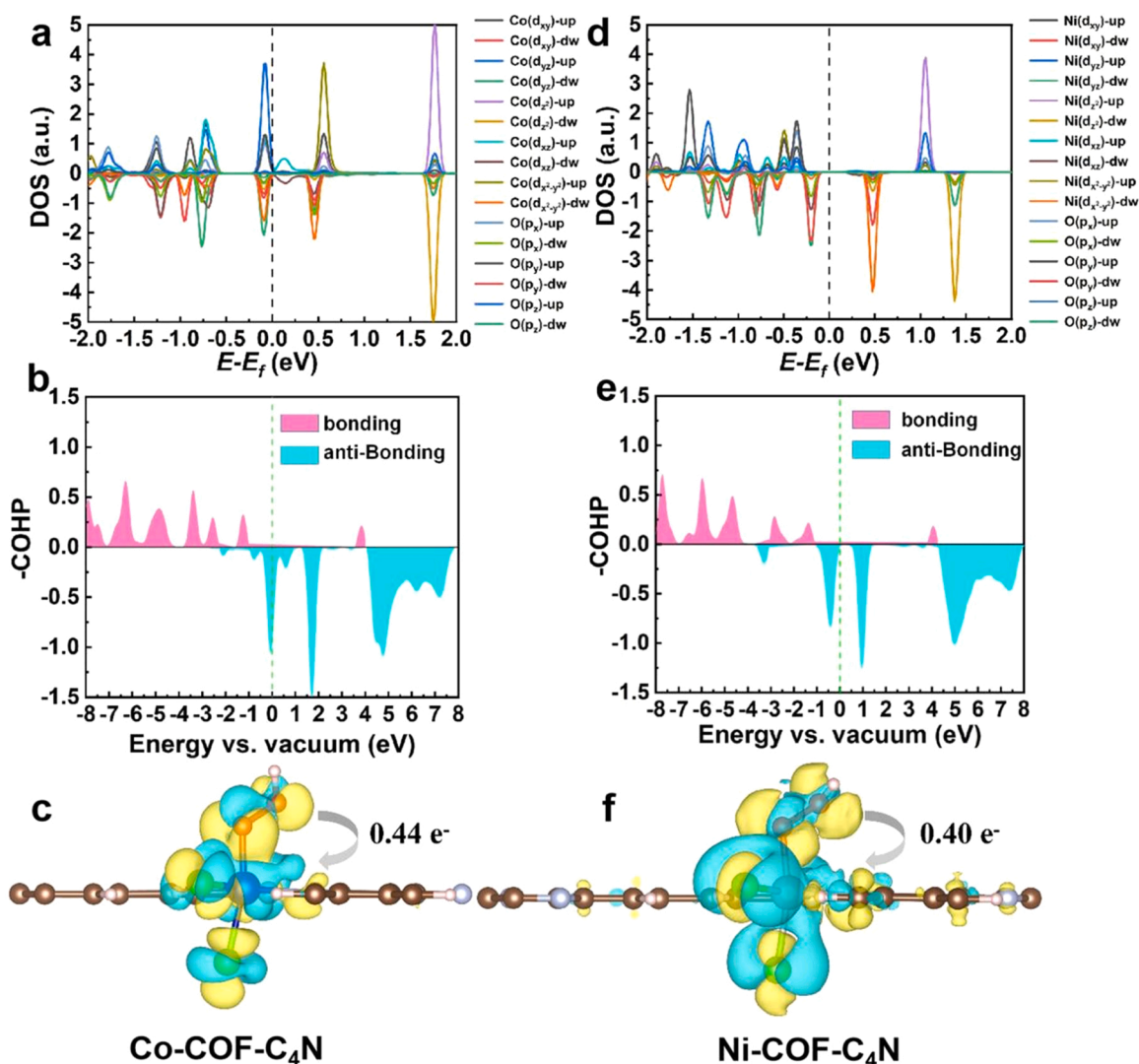


Fig. 9. Electronic structures of Co-COF-C₄N and Ni-COF-C₄N catalysts and orbital interactions between *OOH and TM site of catalysts. Partial density of states of Co (Ni) 3d and O 2p of *OOH intermediate for (a) Co-COF-C₄N and (d) Ni-COF-C₄N, respectively. COHP bonding analysis of the TM-*OOH interaction on the TM active sites of (b) Co-COF-C₄N and (e) Ni-COF-C₄N. The Fermi levels were set to zero energy. The bonding interaction occurs at COHP larger than zero, whereas the anti-bonding interaction occurs at COHP smaller than zero. Charge density difference between *OOH and TM site on (c) Co-COF-C₄N and (f) Ni-COF-C₄N. The yellow and cyan regions represent positive charge accumulation and depletion, and the isosurface value is 0.0009 e Å⁻³.

Co-COF-C₄N gives stronger *OOH adsorption strength due to less anti-bonding states are below E_F . Additionally, the charge density differences between the metal site and *OOH intermediate for Co-COF-C₄N and Ni-COF-C₄N are shown in Fig. 9c and f. The electrons transfer from the *OOH to Co atom is 0.44 |e| due to strong d - $p\pi$ coupling between Co 3d state and O 2p_z state, while only 0.40 |e| electrons transfer from the *OOH atom to Ni. Hence, the positive charges on Co-COF-C₄N are easier to transfer and accumulate on *OOH to activate the OER and to release O₂.

4. Conclusion

In conclusion, we have proposed two generic descriptors to screen the optimal TM atom to be anchored on COF-C₄N's native N-edge cavities as SAC to enhance the OER activity. The two descriptors are examined based on DFT calculations of two periods' TMs for OER associated with various TM-COF-C₄N catalysts. The descriptors suggest the non-precious metal Co and Ni anchored COF-C₄N exhibit the lowest reaction free energy change and theoretical overpotentials among the fourth and fifth periods' TM-COF-C₄N. To verify the theoretical

prediction, both Co-COF-C₄N and Ni-COF-C₄N are selected for the target synthesis. The experimentally measured OER activities of Co-COF-C₄N and Ni-COF-C₄N validate the theoretical predictions. In particular, the OER performance of Co-COF-C₄N is 280 mV at 10 mA cm⁻², 69 mV lower than that of COF-C₄N. And it can provide a current density of up to 399 mA cm⁻², two times higher than that of COF-C₄N, which is superior to the vast majority of previously reported OER electrocatalysts. We find that the key intermediate of the Co-COF-C₄N OER is formed due to the strong d - $p\pi$ coupling and the charge transfer ability. We also find that the proposed descriptors are generic as they can be applicable to other TM anchored COF electrocatalysts.

CRedit authorship contribution statement

Rui Zhang: Theoretical simulation, Data curation, Formal analysis and Writing - theoretical part draft. **Wenshan Liu:** Experimental investigation, Data curation, Formal analysis and Writing- experimental part draft. **Rui Zhang and Wenshan Liu** contributed equally. **Feng-Ming Zhang:** Conceptualization and Methodology. **Zhao-Di Yang:** Supervision, Writing, Project administration and Funding acquisition.

Guiling Zhang: Supervision, Methodology and Funding acquisition.
Xiao Cheng Zeng: Conceptualization, Methodology and Supervision.

Declaration of Competing Interest

The authors declare that they have no known competing financial interests or personal relationships that could have appeared to influence the work reported in this paper.

Data availability

Data will be made available on request.

Acknowledgements

ZDY was financially supported by the Natural Science Foundation of China (52273288 and 51973046) and the Natural Science Foundation of Heilongjiang Province of China (LH2021B014). XCZ acknowledges the support by Hong Kong Global STEM Professorship Scheme.

Appendix A. Supporting information

Supplementary data associated with this article can be found in the online version at doi:10.1016/j.apcatb.2023.122366.

References

- [1] C.-Y. Lin, D. Zhang, Z. Zhao, Z. Xia, Covalent organic framework electrocatalysts for clean energy conversion, *Adv. Mater.* 30 (2017) 1703646.
- [2] X. Feng, X. Ding, D. Jiang, Covalent organic frameworks, *Chem. Soc. Rev.* 41 (2012) 6010–6022.
- [3] Y. Wan, L. Wang, H. Xu, X. Wu, J. Yang, A simple molecular design strategy for two-dimensional covalent organic framework capable of visible-light-driven water splitting, *J. Am. Chem. Soc.* 142 (2020) 4508–4516.
- [4] H. Zhang, M. Zhu, O.G. Schmidt, S. Chen, K. Zhang, Covalent organic frameworks for efficient energy electrocatalysis: rational design and progress, *Adv. Energy Sustain. Res.* 2 (2021) 2000090.
- [5] M.G. Walter, E.L. Warren, J.R. McKone, S.W. Boettcher, Q. Mi, E.A. Santori, N. S. Lewis, Solar water splitting cells, *Chem. Rev.* 110 (2010) 6446–6473.
- [6] J.-T. Ren, Y. Yao, Z.-Y. Yuan, Fabrication strategies of porous precious-metal-free bifunctional electrocatalysts for overall water splitting: recent advances, *Green. Energy Environ.* 6 (2020) 620–643.
- [7] J. Diao, Y. Qiu, S. Liu, W. Wang, K. Chen, H. Li, W. Yuan, Y. Qu, X. Guo, Interfacial engineering of W_2N/WC heterostructures derived from solid-state synthesis: a highly efficient trifunctional electrocatalyst for ORR, OER, and HER, *Adv. Mater.* 32 (2020) 1905679.
- [8] J. Guan, Z. Duan, F. Zhang, S.D. Kelly, R. Si, M. Dupuis, Q. Huang, J.Q. Chen, C. Tang, C. Li, Water oxidation on a mononuclear manganese heterogeneous catalyst, *Nat. Catal.* 1 (2018) 870–877.
- [9] S. Sadtler, G. Bendt, S. Salamon, F.T. Haase, J. Landers, J. Timoshenko, C. Rettenmaier, H.S. Jeon, A. Bergmann, H. Wende, B.R. Cuenya, S. Schulz, Influence of the cobalt content in cobalt iron oxides on the electrocatalytic OER, *Act., J. Mater. Chem. A* 9 (2021) 25381.
- [10] T. Ouyang, Y.-Q. Ye, C.-Y. Wu, K. Xiao, Z.-Q. Liu, Heterostructures composed of N-doped carbon nanotubes encapsulating cobalt and b-Mo₂C nanoparticles as bifunctional electrodes for water splitting, *Angew. Chem. Int. Ed.* 58 (2019) 4923–4928.
- [11] J. Tang, C. Su, Z. Shao, Covalent organic framework (COF)-based hybrids for electrocatalysis: recent advances and perspectives, *Small Methods* 5 (2021) 2100945.
- [12] H. Hu, Q. Yan, R. Ge, Y. Gao, Covalent organic frameworks as heterogeneous catalysts, *Chin. J. Catal.* 39 (2018) 1167–1179.
- [13] Y. Cao, W. Peng, F. Zhang, Y. Zhu, X. Fan, Atomically dispersed metal sites in COF-based nanomaterials for electrochemical energy conversion, *Green. Energy Environ. Press* (2021).
- [14] X. Cui, S. Lei, A.C. Wang, L. Gao, Q. Zhang, Y. Yang, Z. Lin, Emerging covalent organic frameworks tailored materials for electrocatalysis, *Nano Energy* 70 (2020), 104525.
- [15] Y. Wang, H. Yuan, Y. Li, Z. Chen, Two-dimensional iron-phthalocyanine (Fe-Pc) monolayer as a promising single-atom-catalyst for oxygen reduction reaction: a computational study, *Nanoscale* 7 (2015) 11633.
- [16] S. Huang, K. Chen, T.-T. Li, Porphyrin and phthalocyanine based covalent organic frameworks for electrocatalysis, *Coord. Chem. Rev.* 464 (2022), 214563.
- [17] Y. Kim, D. Kim, J. Lee, L.Y.S. Lee, D.K.-P. Ng, Tuning the electrochemical properties of polymeric cobalt phthalocyanines for efficient water splitting, *Adv. Funct. Mater.* 31 (2021) 2103290.
- [18] A. Singh, S. Roy, C. Das, D. Samanta, T.K. Maji, Metallophthalocyanine-based redox active metal-organic conjugated microporous polymers for OER catalysis, *Chem. Commun.* 54 (2018) 4465.
- [19] W.-K. Jo, S. Moru, S. Tonda, Cobalt-coordinated sulfur-doped graphitic carbon nitride on reduced graphene oxide: an efficient metal–(N,S)–C-class bifunctional electrocatalyst for overall water splitting in alkaline media, *ACS Sustain. Chem. Eng.* 7 (2019) 15373–15384.
- [20] C.-Y. Lin, L. Zhang, Z. Zhao, Z. Xia, Design principles for covalent organic frameworks as efficient electrocatalysts in clean energy conversion and green oxidizer production, *Adv. Mater.* 29 (2017) 1606635.
- [21] Y. Zheng, Y. Jiao, Y. Zhu, Q. Cai, A. Vasileff, L.H. Li, Y. Han, Y. Chen, S.-Z. Qiao, olecule-Level g-C₃N₄ coordinated transition metals as a new class of electrocatalysts for oxygen electrode reactions, *J. Am. Chem. Soc.* 139 (2017) 3336–3339.
- [22] S. Nandi, S.K. Singh, D. Mullangi, R. Illathvalappil, L. George, C.P. Vinod, S. Kurugot, R. Vaidyanathan, Low band gap benzimidazole COF supported Ni₃N as highly active OER catalyst, *Adv. Energy Mater.* 6 (2016) 1601189.
- [23] K. Geng, T. He, R. Liu, S. Dalapati, K.T. Tan, Z. Li, S. Tao, Y. Gong, Q. Jiang, D. Jiang, Covalent organic frameworks: design, synthesis, and functions, *Chem. Rev.* 120 (2020) 8814–8933.
- [24] D. Zhao, Z. Zhuang, X. Cao, C. Zhang, Q. Peng, C. Chen, Y. Li, Atomic site electrocatalysts for water splitting, oxygen reduction and selective oxidation, *Chem. Soc. Rev.* 49 (2020) 2215–2264.
- [25] S. Mondal, B. Mohanty, M. Nurhuda, S. Dalapati, R. Jana, M. Addicoat, A. Datta, B. K. Jena, A. Bhaumik, A. Thiadiazole-based, Covalent organic framework: a metal-free electrocatalyst toward oxygen evolution reaction, *ACS Catal.* 10 (2020) 5623–5630.
- [26] A. Allangwi, T. Mamood, K. Ayub, M.A. Gilani, Anchoring the late first row transition metals with B12P12 nanocage to act as single atom catalysts toward oxygen evolution reaction (OER), *Mater. Sci. Semicond. Proc.* 153 (2023), 107164.
- [27] F. Ullah, K. Ayub, T. Mahmood, High performance SACs for HER process using late first-row transition metals anchored on graphyne support: a DFT insight, *Int. J. Hydrog. Energy* 46 (2021) 37814–37823.
- [28] H.B. Aiyappa, J. Thote, D.B. Shinde, R. Banerjee, S. Kurugot, Cobalt modified covalent organic framework as a robust water oxidation electrocatalyst, *Chem. Mater.* 28 (2016) 4375–4379.
- [29] Q. Pan, M. Abdellah, Y. Cao, W. Lin, Y. Liu, J. Meng, Q. Zhou, Q. Zhao, X. Yan, Z. Li, H. Cui, H. Cao, W. Fang, D.A. Tanner, M. Abdel-Hafiez, Y. Zhou, T. Pullerits, S.E. Canton, H. Xu, K. Zheng, Ultrafast charge transfer dynamics in 2D covalent organic frameworks/Re-complex hybrid photocatalyst, *Nat. Comm.* 13 (2022) 845.
- [30] X.-F. Yang, A. Wang, B. Qiao, J. Li, J. Liu, T. Zhang, Single-atom catalysts: a new frontier in heterogeneous catalysis, *Acc. Chem. Res.* 46 (2013) 1740–1748.
- [31] D. Wu, Q. Xu, J. Qian, X. Li, Y. Sun, Bimetallic covalent organic frameworks for constructing multifunctional electrocatalyst, *Chem. Eur. J.* 25 (2019) 3105–3111.
- [32] T. Hosokawa, M. Tsuji, K. Tsuchida, K. Iwase, T. Harada, S. Nakanishi, K. Kamiya, Metal-doped bipyridine linked covalent organic framework films as a platform for photoelectrocatalysts, *J. Mater. Chem. A* 9 (2021) 11073–11080.
- [33] C. Yang, Z.-D. Yang, H. Dong, N. Sun, Y. Lu, F.-M. Zhang, G. Zhang, Theory-driven design and targeting synthesis of a highly-conjugated basal-plane 2D covalent organic framework for metal-free electrocatalytic OER, *ACS Energy Lett.* 4 (2019) 2251–2258.
- [34] R. Zhang, W. Jian, Z.-D. Yang, F.-Q. Bai, Insights into the photocatalytic mechanism of the C₄N/MoS₂ heterostructure: a first-principle study, *Chin. Chem. Lett.* 31 (2020) 1319–1324.
- [35] H. Xu, D. Cheng, D. Cao, X.C. Zeng, A. Universal, Principle for a rational design of single-atom electrocatalysts, *Nat. Catal.* 1 (2018) 339–348.
- [36] J. Ma, Q. Zhi, L. Gong, Y. Shen, D. Sun, Y. Guo, L. Zhang, Z.A. Xia, Universal descriptor based on pz-orbitals for the catalytic activity of multi-doped carbon bifunctional catalysts for oxygen reduction and evolution, *Nanoscale* 12 (2020) 19375.
- [37] G. Kresse, J. Furthmüller, Efficiency of ab-initio total energy calculations for metals and semiconductors using a plane-wave basis set, *Comput. Mater. Sci.* 6 (1996) 15–20.
- [38] G. Kresse, J. Furthmüller, Efficient iterative schemes for ab initio total-energy calculations using a plane-wave basis set, *Phys. Rev. B* 54 (1996) 11169–11186.
- [39] P.E. Blöchl, Projector augmented-wave method, *Phys. Rev. B* 50 (1994) 1795–17979.
- [40] G. Kresse, D. Joubert, From ultrasoft pseudopotentials to the projector augmented-wave method, *Phys. Rev. B* 59 (1999) 1758–1779.
- [41] J.P. Perdew, K. Burke, M. Ernzerhof, Generalized gradient approximation made simple, *Phys. Rev. Lett.* 77 (1996) 3865–3868.
- [42] S. Grimme, Semiempirical GGA-type density functional constructed with a long-range dispersion correction, *J. Comput. Chem.* 27 (2006) 1787–1799.
- [43] J.K. Nørskov, J. Rossmeisl, A. Logadottir, L. Lindqvist, J.R. Kitchin, T. Bligaard, H. Jónsson, Origin of the overpotential for oxygen reduction at a fuel-cell cathode, *J. Phys. Chem. B* 108 (2004) 17886–17892.
- [44] A.A. Peterson, F. Abild-Pedersen, F. Studt, J. Rossmeisl, J.K. Nørskov, How copper catalyzes the electroreduction of carbon dioxide into hydrocarbon fuels, *Energy Environ. Sci.* 3 (2010) 1311–1315.
- [45] G. Ertl, S.B. Lee, W. Weiss, Kinetics of nitrogen adsorption on Fe(111), *Surf. Sci.* 114 (1982) 515–526.
- [46] J. De Paula, Atkins' Physical Chemistry, Oxford University Press, Oxford, 2010.
- [47] N. Zhang, X. Feng, D. Rao, X. Deng, L. Cai, B. Qiu, R. Long, Y. Xiong, Y. Lu, Y. Chai, Lattice oxygen activation enabled by high-valence metal sites for enhanced water oxidation, *Nat. Commun.* 11 (2020) 1–11.

- [48] Y. Hou, M. Qiu, M.G. Kim, P. Liu, G. Nam, T. Zhang, X. Zhuang, B. Yang, J. Cho, M. Chen, C. Yuan, L. Lei, X. Feng, Atomically dispersed nickel-nitrogen-sulfur species anchored on porous carbon nanosheets for efficient water oxidation, *Nat. Commun.* 10 (2019) 1–9.
- [49] Y. Jiao, Y. Zheng, M. Jaroniec, S.Z. Qiao, Origin of the electrocatalytic oxygen reduction activity of graphene-based catalysts: a roadmap to achieve the best performance, *J. Am. Chem. Soc.* 136 (2014) 4394–4403.
- [50] J. Du, T. Zhang, J. Xing, C. Xu, Hierarchical porous $\text{Fe}_3\text{O}_4/\text{Co}_3\text{S}_4$ nanosheets as an efficient electrocatalyst for the oxygen evolution reaction, *J. Mater. Chem. A* 5 (2017) 9210–9216.
- [51] J. Wang, M. Zheng, X. Zhao, W. Fan, Structure-performance descriptors and the role of the axial oxygen atom on M-N₄-C single-atom catalysts for electrochemical CO_2 reduction, *ACS Catal.* 12 (2022) 5441–5454.
- [52] B. Hammer, J.K. Nørskov, Theoretical surface science and catalysis-calculations and concepts, *Adv. Catal.* 45 (2000) 71–129.
- [53] B. Hammer, J.K. Nørskov, Electronic factors determining the reactivity of metal surfaces, *Surf. Sci.* 343 (1995) 211–220.
- [54] H. Yang, F. Li, S. Zhan, Y. Liu, W. Li, Q. Meng, A. Kravchenko, T. Liu, Y. Yang, Y. Fang, L. Wang, J. Guan, I. Furó, M.S.G. Ahlquist, L. Sun, Intramolecular hydroxyl nucleophilic attack pathway by a polymeric water oxidation catalyst with single cobalt sites, *Nat. Cat.* 5 (2022) 414–429.
- [55] H. Niu, Z. Zhang, X. Wang, X. Wan, C. Shao, Y. Guo, Theoretical Insights into the mechanism of selective nitrate-to-ammonia electroreduction on single-atom catalysts, *Adv. Funct. Mater.* 31 (2021) 2008533.
- [56] X. Liu, Y. Jiao, Y. Zheng, M. Jaroniec, S.-Z. Qiao, Building up a picture of the electrocatalytic nitrogen reduction activity of transition metal single atom catalysts, *J. Am. Chem. Soc.* 141 (2019) 9664–9672.